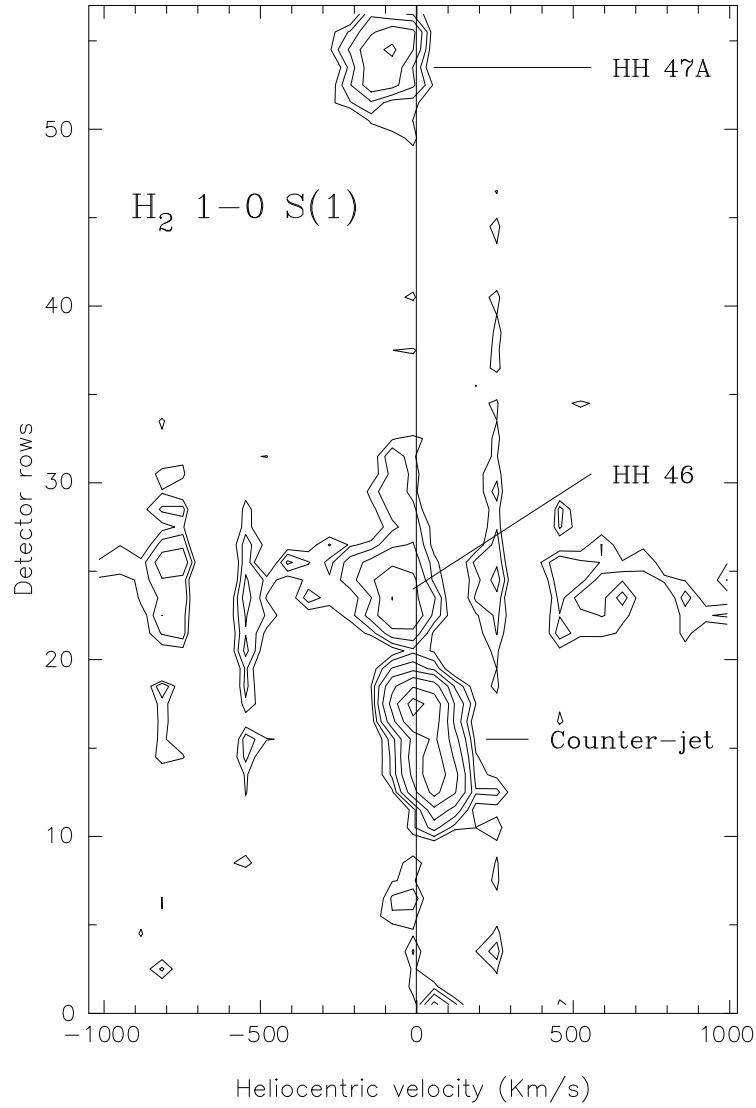
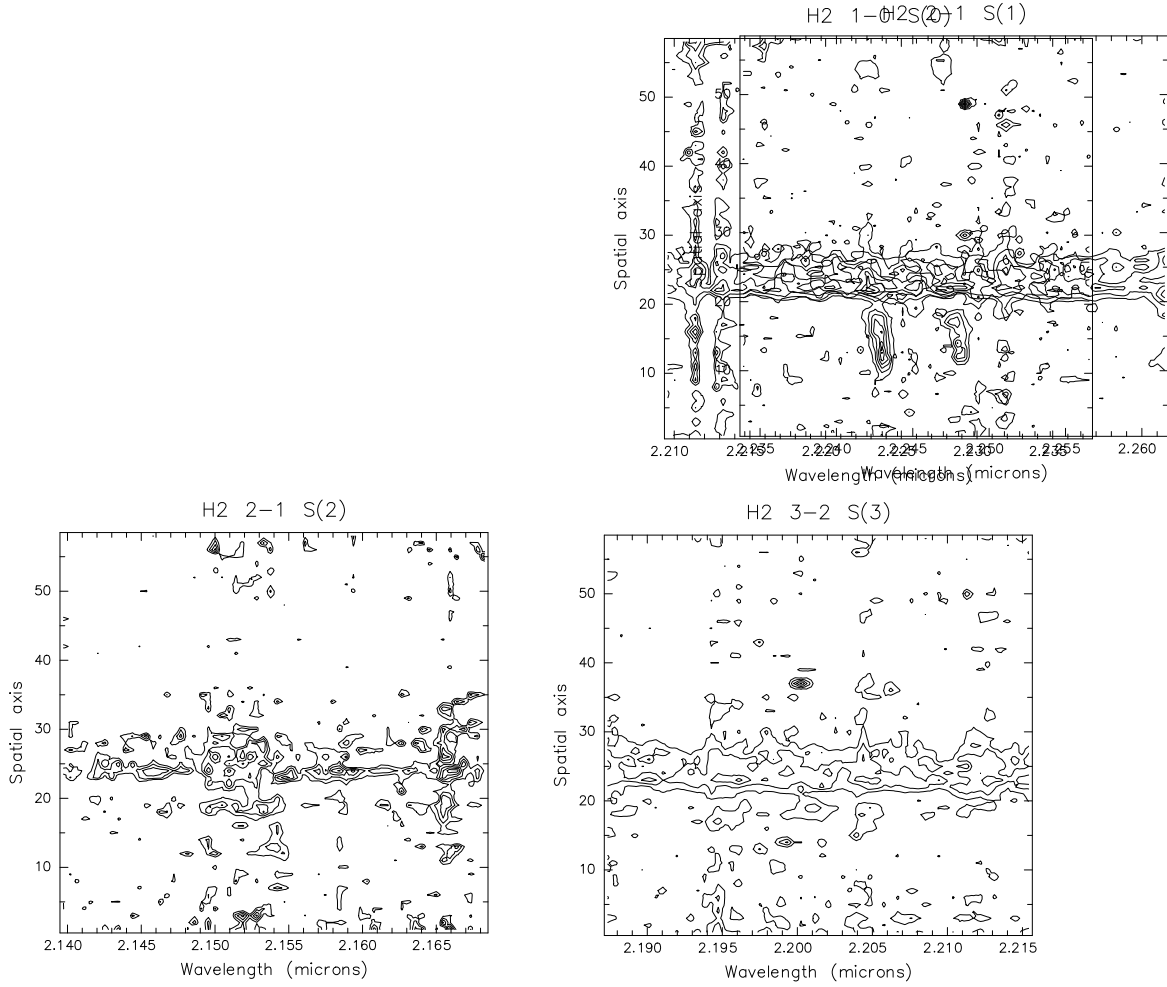


**Figure 1.** Image of the region studied in the HH46/47 complex. The observed slit position is shown superposed on a [SII]  $0.673 \mu\text{m}$  plus  $\text{H}_2$  1-0 S(1)  $2.12 \mu\text{m}$  (contours) map. Adapted from Eislöffel et al. (1994).



**Figure 2.** Near-infrared contour emission map obtained for the H<sub>2</sub> 1-0 S(1) transition on the HH46/47 object. The position of the HH objects are labelled in this figure, as well as the bright and extended counter-jet flow. The spatial co-ordinate is given in IRSPEC rows (each corresponding to a length of 2.2'' per pixel on the sky) on the left axis. To plot this image, we used 7 contours increasing in steps of  $\sqrt{2}$  from a base level of  $0.25 \times 10^{-11} \text{ erg s}^{-1} \text{ cm}^{-2} \mu\text{m}^{-1}$ . The vertical line is plotted at zero heliocentric radial velocity.



**Figure 3.** Position-velocity emission maps obtained for the higher excitation H<sub>2</sub> line emission discussed in the main text. The 2-1S(1) transition has contours plotted linearly from a base contour of  $0.09 \times 10^{-11} \text{ergs}^{-1} \text{cm}^{-2} \mu\text{m}^{-1}$ , and stepped by  $0.05 \times 10^{-11} \text{ergs}^{-1} \text{cm}^{-2} \mu\text{m}^{-1}$ . The 1-0S(0) transition has contours plotted linearly from a base contour of  $0.13 \times 10^{-11} \text{ergs}^{-1} \text{cm}^{-2} \mu\text{m}^{-1}$ , and stepped by  $0.07 \times 10^{-11} \text{ergs}^{-1} \text{cm}^{-2} \mu\text{m}^{-1}$ . The 2-1S(2) transition has contours plotted linearly from a base contour of  $0.11 \times 10^{-11} \text{ergs}^{-1} \text{cm}^{-2} \mu\text{m}^{-1}$ , and stepped by  $0.025 \times 10^{-11} \text{ergs}^{-1} \text{cm}^{-2} \mu\text{m}^{-1}$ . The 3-2 S(3) transition has contours plotted linearly from a base contour of  $0.16 \times 10^{-11} \text{ergs}^{-1} \text{cm}^{-2} \mu\text{m}^{-1}$ , and stepped by  $0.02 \times 10^{-11} \text{ergs}^{-1} \text{cm}^{-2} \mu\text{m}^{-1}$ .

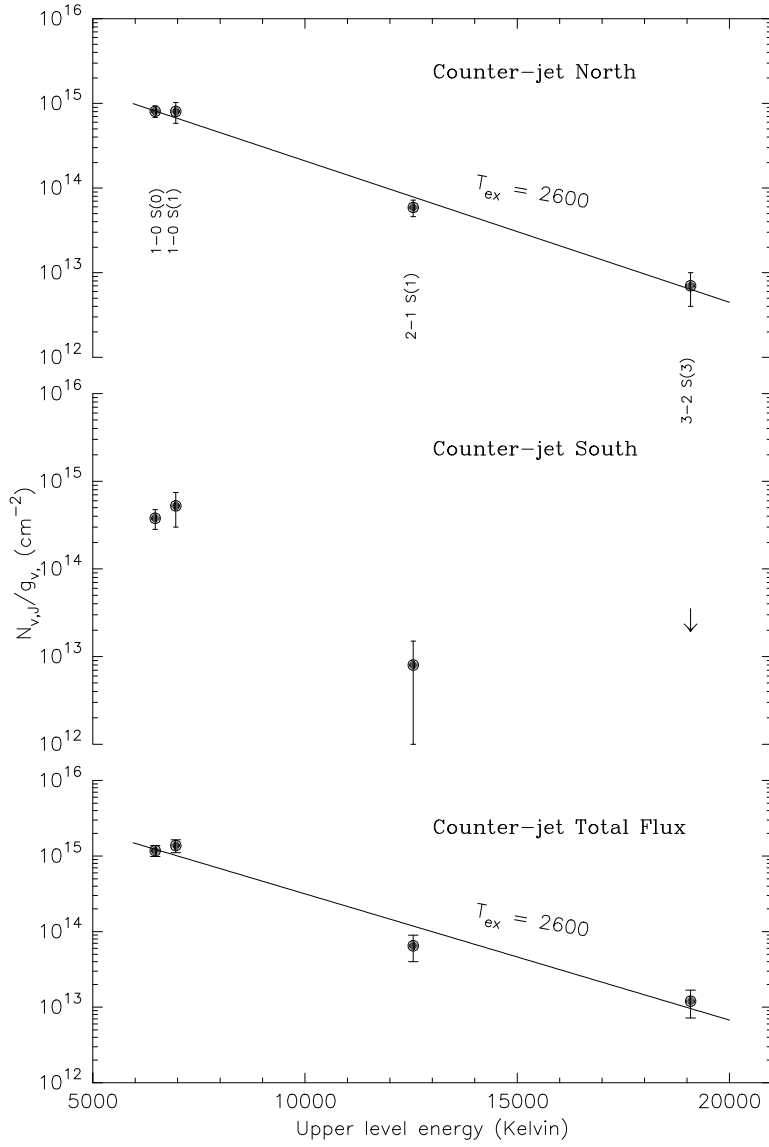


**Figure 4.** H<sub>2</sub> excitation diagrams for the counter-jet. The dereddened column densities are plotted against the transition upper level energy for the four H<sub>2</sub> lines (labelled next to the plotted data point) observed with the highest signal-to-noise (see Table 3). The arrow in the plot represents a 3 $\sigma$  upper limit. The solid line represents the least squares fit to the errorless data points providing an excitation temperature of  $T_{\text{ex}} = 2600$  K ( $\pm 300$  K) for the whole counter-jet (Total; bottom diagram) and the northern peak in the counter-jet (North; top diagram)

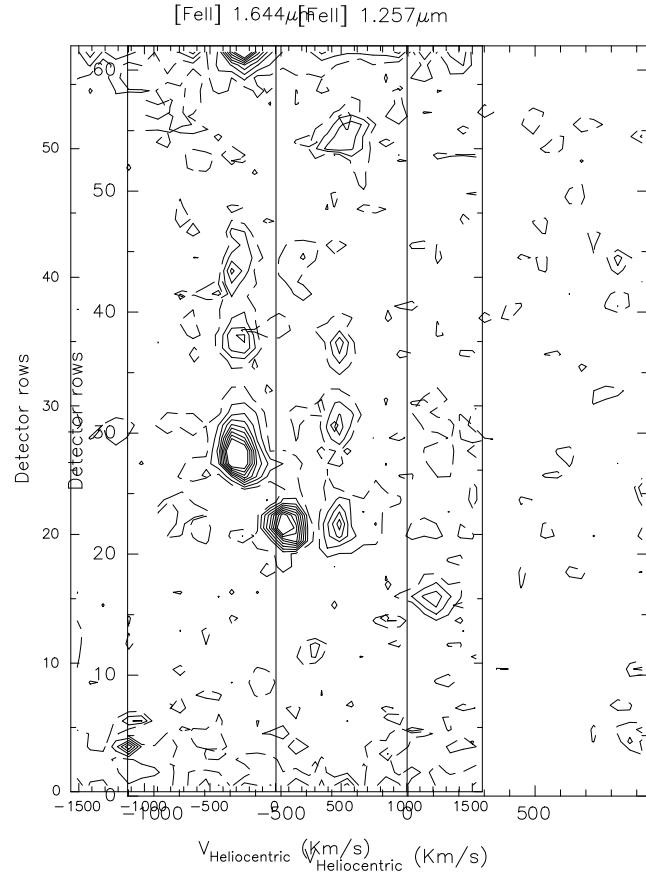


**Figure 5.** Position-velocity emission maps obtained in the [Fe II] 1.257  $\mu\text{m}$  and [Fe II] 1.644  $\mu\text{m}$  transitions. For the [Fe II] 1.644  $\mu\text{m}$ , the base contour is plotted at  $0.55 \times 10^{-11} \text{erg s}^{-1} \text{cm}^{-2} \mu\text{m}^{-1}$  with a linear step of  $0.15 \times 10^{-11} \text{erg s}^{-1} \text{cm}^{-2} \mu\text{m}^{-1}$  whereas for the [Fe II] 1.257  $\mu\text{m}$ , the base contour is at  $1.1 \times 10^{-11} \text{erg s}^{-1} \text{cm}^{-2} \mu\text{m}^{-1}$  and adjacent contours are stepped linearly by  $0.7 \times 10^{-11} \text{erg s}^{-1} \text{cm}^{-2} \mu\text{m}^{-1}$ . In both maps, the vertical solid lines are drawn at zero velocity emission whereas the horizontal solid lines is drawn at the position of the continuum emission from the HH46 object. These positions have been calculated using the spatial offsets given in Table 1.

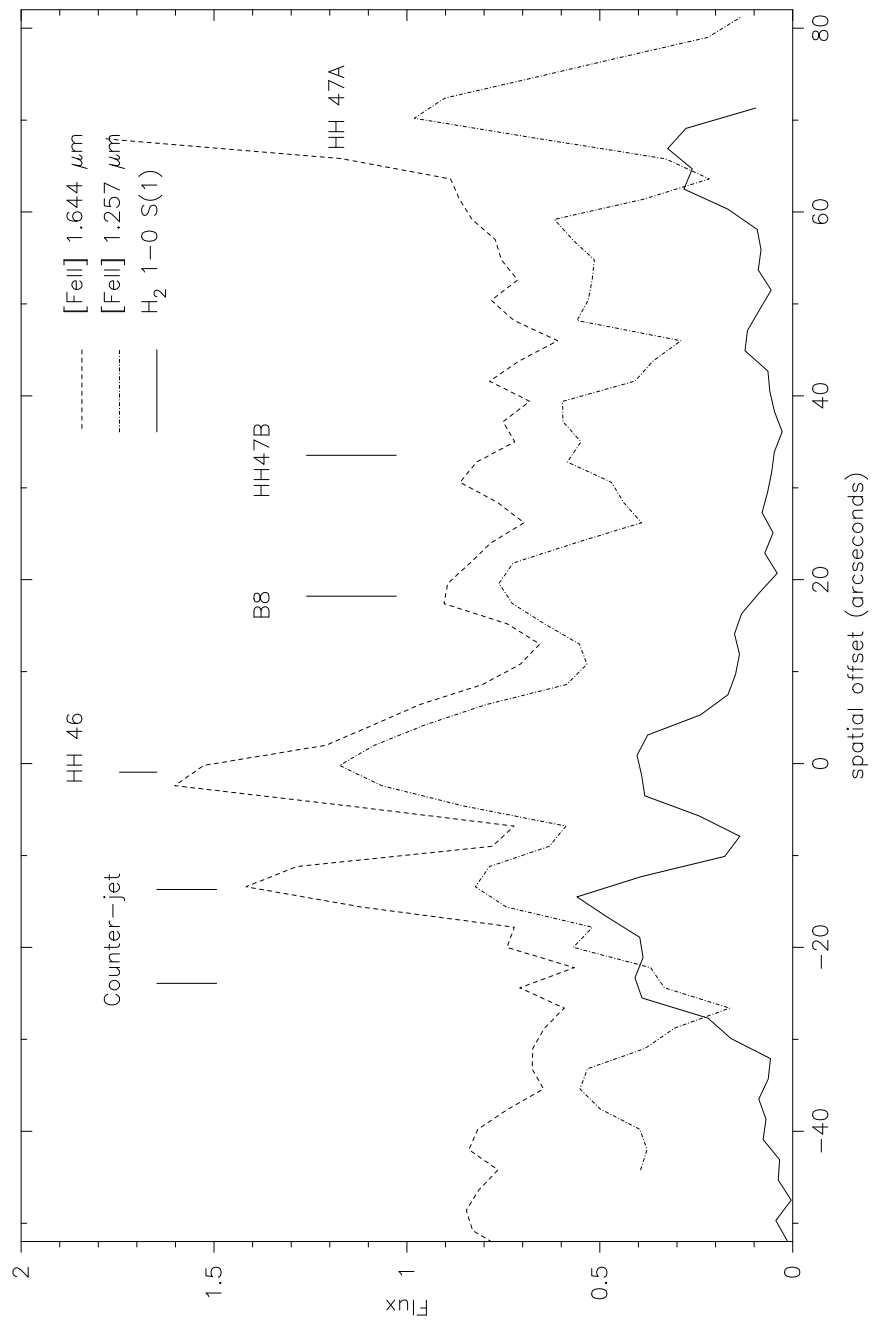


**Figure 6.** Spatial emission profiles of the observed slit.

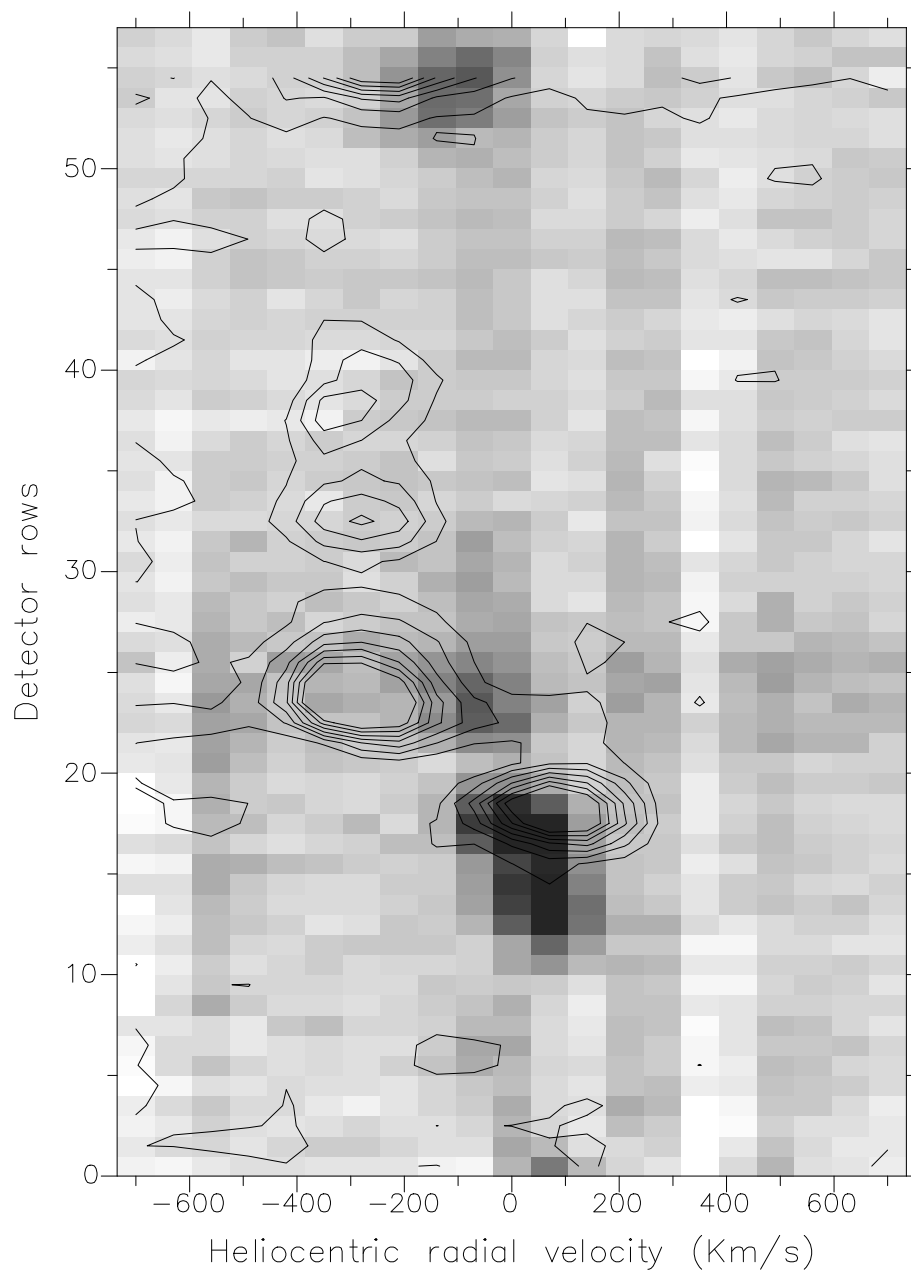


**Figure 7.** Overlay of the  $\text{H}_2$  1-0 S(1) and  $[\text{Fe II}]$  1.644  $\mu\text{m}$  emission maps.

# The excitation and kinematical properties of $\text{H}_2$ and $[\text{Fe II}]$ in the HH 46/47 bipolar outflow<sup>\*</sup>

A.J.L. Fernandes

*E-mail:* amadeu@astro.up.pt

*Centro de Astrofísica da Universidade do Porto, Rua das Estrelas, 4150-762 Porto, Portugal*

*Instituto Superior da Maia, Portugal*

5 November 2018

## ABSTRACT

Long slit spectra of the molecular outflow Herbig-Haro (HH) 46/47 has been taken in the J and K near-infrared bands. The observed  $\text{H}_2$  line emission confirms the existence of a bright and extended redshifted counter-jet outflow southwest of HH46. We show that this outflow seems to be composed of two different emission regions which have distinct heliocentric velocities, in contrast with the optical appearance, and which implies an acceleration of the counter-jet.

The observed  $[\text{Fe II}]$  emission suggests an average extinction of 7–9 visual magnitudes for the region associated with the counter-jet.

Through position-velocity diagrams, we show the existence of different morphologies for the  $\text{H}_2$  and  $[\text{Fe II}]$  emission regions in the northern part of the HH 46/47 outflow. We have detected for the first time high velocity ( $-250 \text{ km s}^{-1}$ )  $[\text{Fe II}]$  emission in the region bridging HH46 to HH47A. The two strong peaks detected can be identified with the optical positions B8 and HH47B.

The  $\text{H}_2$  excitation diagrams for the counter-jet shock suggest an excitation temperature for the gas of  $T_{\text{ex}} \approx 2600$ . The lack of emission from the higher energy  $\text{H}_2$  lines such as the 4-3 S(3) transition, suggests a thermal excitation scenario for the origin of the observed emission. Comparison of the  $\text{H}_2$  line ratios to various shock models yielded useful constraints about the geometry and type of these shocks. Planar shocks can be ruled out whereas curved or bow-shocks (both J and C-type) can be parametrised to adjust our data.

**Key words:** ISM: individual objects: HH46/47 – ISM: jets and outflows – ISM: kinematics and dynamics – Infrared: ISM: lines and bands

## 1 INTRODUCTION

For its tight spatial alignment of the emission knots and its clear visibility against the progenitor dark globule, HH 46/47 is one of the most remarkable examples of the classical Herbig-Haro object. Being optically bright, this HH complex has been the subject of many studies of its spectral, photometric and kinematical properties after its discovery by Schwartz (1977).

The morphology of the Gum nebula region (Dopita et al. 1982) shows the existence of a very collimated jet that is composed of several components which extend about 0.39 pc on the sky at the assumed distance of 350 pc (Eisloffel and Mundt 1994). A young T Tauri star still obscured by

the surrounding dust envelope sits at the center of this system. This star illuminates a cloud of dust revealing a reflection nebula from which the optically visible HH 46 and HH 47(A,B,C,D) jet components emerge.

The bipolar nature of this outflow was first ascertained by Graham and Elias (1983), on discovering blue and redshifted outflowing shocked gas to either side of the central source. Schwartz et al. (1984) reported the first proper motions for some dense knots along the flow suggesting the occurrence of episodic ejections of gas material from the energy source. Combining the radial velocity measurements (Meaburn & Dyson 1987, Hartigan et al. 1993, Morse et al 1994) with a detailed study of the proper motions of the knots in the HH 46/47 jet (Eisloffel & Mundt 1994), a space velocity of about  $300 \text{ km s}^{-1}$  is found for the jet.

While several imaging, spectroscopic and proper motion studies have been carried out in the optical for the

<sup>\*</sup> Based on observations collected at the European Southern Observatory, La Silla, Chile



blueshifted part of HH 46/47, there has been considerably less work done for the redshifted part of the flow. This well-collimated counter-jet flow located southwest of the source was discovered by Reipurth and Heathcote (1991) in [SII]  $\lambda\lambda 6717/6731$  line emission and found to be redshifted with a heliocentric radial velocity of about  $+125 \text{ km s}^{-1}$ . K-band imaging of the redshifted counter-flow has been performed by Eisloffel et al. (1994), together with  $\text{H}_2$  1-0 S(1) ( $2.1218 \mu\text{m}$ ) and [Fe II] ( $1.644 \mu\text{m}$ ) line imaging. More recently, proper motion studies of the  $\text{H}_2$  emission have been carried out for the  $\text{H}_2$  knots in HH 46/47 (Micono et al. 1998).

## 2 OBSERVATIONS AND DATA REDUCTION

The HH 46/47 complex was observed in 1995 March 14 to 17 using the cryogenically cooled grating spectrometer IR-SPEC installed on the ESO 3.5 m New Technology Telescope (NTT) sited at La Silla, Chile. The instrument was equipped with an InSb CCD detector comprising  $58 \times 62$  square pixels which provided a pixel scale of 2.2 arcseconds on the sky. We have positioned the 2 arcminute long  $\times$  2.2 arcseconds wide slit at a position angle of 57 degrees over the HH 46/47 bipolar flow, centered on approximately the HH 46 emission nebula continuum (Figure 1). This orientation on the sky coincides with the outflow axis of both optical and infrared maps of HH 46/47 and the 2 arcminute long slit allowed us to measure simultaneously the emission region from the HH 47A object to the counter-jet flow. The precise positioning of the observed slit position was set by peaking up the  $\text{H}_2$  emission maximum. The telescope pointing accuracy, normally better than  $1''$  (Moorwood et al. 1991) has been checked with observations of the standard stars.

The seeing disk remained under  $1''$  with an average FWHM of  $0.8''$ . Grating no. 2 was used with the slit set to a width of 2 pixels. The spectral resolution was  $\sim 0.001 \mu\text{m}$  (FWHM) at  $2.122 \mu\text{m}$  but varied little over the whole K band region ( $R = \lambda/\Delta\lambda \approx 2300$ ). For the two observed [Fe II] transitions, the resolution was  $R \approx 3300$  and  $1600$  at  $1.257 \mu\text{m}$  and  $1.644 \mu\text{m}$ , respectively. At these resolutions, every frame contained a very short wavelength range and only one emission line was registered per frame. Because of the extent of the HH 46/47 outflow on the  $2'$  slit, explicit sky observations were taken by offsetting the telescope  $40''$  south from the nominal object position. The integration times were 60 seconds on source and 60 seconds on sky and a final frame was determined by averaging many integrations. The observational procedure consisted in taking several exposures at the different programme wavelengths on each night and then coadding them to produce a higher signal-to-noise final frame. The observations were performed on the following emission lines of  $\text{H}_2$  arising in the K band;  $v=1-0$  S(1) [ $2.1218 \mu\text{m}$ ],  $1-0$  S(0) [ $2.2235 \mu\text{m}$ ],  $2-1$  S(1) [ $2.2477 \mu\text{m}$ ],  $2-1$  S(2) [ $2.1540 \mu\text{m}$ ],  $2-1$  S(3) [ $2.0650 \mu\text{m}$ ],  $3-2$  S(1) [ $2.3846 \mu\text{m}$ ],  $3-2$  S(3) [ $2.2014 \mu\text{m}$ ], and the  $4-3$  S(3) [ $2.3445 \mu\text{m}$ ]. In addition, we have observed the  $\text{Br}\gamma$  transition at  $2.166 \mu\text{m}$  and two emission lines of iron: [Fe II]  $1.257 \mu\text{m}$  and [Fe II]  $1.644 \mu\text{m}$  arising on the J and H bands, respectively. Table 1 provides a list of all the line observations together with the observational parameters for each line transition.

One of the main goals of the project was to observe the high-excitation  $\text{H}_2$  lines (with upper level energies above 13000 K) of molecular hydrogen in the K band, especially the ones arising from vibrational levels  $v'=3$  (e.g. the  $3-2$  S(3) [ $2.2014 \mu\text{m}$ ]) and  $v'=4$  (e.g. the  $4-3$  S(3) [ $2.3445 \mu\text{m}$ ]). Making exposures at such low-light levels that are characteristic of these faint lines in shocked regions required a special technique since several effects such as the non-linearity of the array at low-light levels may be comparable with the photon noise level (Gredel and Moorwood 1991). The method employed consisted in taking several frames at the same wavelength but slightly shifted by  $1/2$  and  $1$  pixel, thus ensuring that the same flux is sampled by different pixels on the array. This also helps to prevent the spread of bad pixels to the final image. To produce the final reduced image we align the frames to a common wavelength grid and coadd up the exposures to gain sufficient signal-to-noise on the emission line.

Three photometric standard stars were routinely observed throughout the night at the same object wavelengths and airmass to allow a proper cancellation of telluric absorption features and to flux calibrate the object. The stars observed were: Beta Car (HR 3685), Eta Cma (HR 2827) and Iota Car (HR 3699). The relative variation of the standard star flux over the three night period, provided an estimate of the uncertainty on the calculated flux of  $\sim 10\%$ . After inspecting the reduced standard star frames, we noted that at two wavelengths, the standard star continuum displayed deep absorption features at  $2.166 \mu\text{m}$  and  $1.642 \mu\text{m}$ . These features are known to be associated with the absorption by the stellar photosphere of the hydrogen recombination radiation. The lines in question are the H I [ $n=7-4$ ] and H I [ $n=12-4$ ], for the  $2.166 \mu\text{m}$  and  $1.642 \mu\text{m}$ , respectively and were artificially removed by linear interpolation between the line edges, a common practice since the error committed is negligible compared to the star's continuum absolute flux.

The flux calibration procedure required a flux table for each standard containing a properly sampled representation ( $\lambda$  vs. flux) of the continuum for each standard star. Such file was constructed for each star based on the broad band flux given in the SIMBAD<sup>†</sup> database. Using this table, it is possible to reproduce the star's flux distribution over the wavelength region of interest and to use this curve to calibrate the flux counts in the object frames. All data were primarily reduced with specific ESO routines available in MIDAS for IRSPEC observations. The later stages of data reduction that include standard procedures (sky subtraction, flat-fielding, wavelength and flux calibration) were assisted with routines from the STARLINK project.

With the current IRSPEC standard setup, a slight spatial displacement of the objects occurs between frames taken at different wavelength settings. This is known to be caused by changing the grating settings between the different exposures (Gredel and Moorwood 1991). Thus, in order to correct for this effect, we have determined the relative spatial shift between the different wavelengths frames by calculating the centroid position in the spatial direction for the observed star continuum. This was achieved by fitting a gaussian (in-

<sup>†</sup> The SIMBAD database is operated by the Centre de Données astronomiques de Strasbourg, France

strumental spatial profile) to the spatial profile of the star's image for all wavelengths. We found a shift of +3.5 pixels for the [Fe II] 1.257  $\mu\text{m}$  image map and of -2.5 pixels for the [Fe II] 1.644  $\mu\text{m}$  image map relatively to the H<sub>2</sub> 1-0 S(1) map. All the other H<sub>2</sub> lines have intermediate shifts ranging from -0.5 at 2.065  $\mu\text{m}$  to +2.5 at 2.3846  $\mu\text{m}$ . All the calculated spatial shifts between the frames are shown in column 5 of Table 1.

### 3 RESULTS

A total of eight H<sub>2</sub> transitions were observed during the first two nights. These arise from vibrational levels:  $v=1, 2, 3$  and 4, and have all rotational jumps of  $\Delta J = +2$ . Table 1 shows the parameter list of the observed emission lines. For each line observed, this table shows in the fourth column the total exposure time of the final reduced frame. In addition, the fifth and sixth columns give respectively, the spatial shift used to correct the different grating settings to the same offset and the velocity resolution for each frame.

The heliocentric velocity correction for the time the observations were performed ( $-3 \text{ km s}^{-1}$ ) is negligible when compared with the width of a pixel ( $48\text{--}98 \text{ km s}^{-1}$ ). Thus, we have chosen not to make any corrections on the calculated position-velocity maps after converting the wavelength scale to the radial velocity scale on the maps. This conversion was applied only to the H<sub>2</sub> 1-0 S(1) and the two [Fe II] maps since only these are bright enough to compute the radial velocity of emitting gas. The velocities are thus measured with respect to the Bok globule which is believed to have a heliocentric radial velocity  $\sim +22 \text{ km s}^{-1}$  (Hartigan et al. 1993).

#### 3.1 The line emission

Figure 2 shows the position-velocity contour emission map observed for the H<sub>2</sub> 1-0 S(1) transition at 2.1218  $\mu\text{m}$ . This transition is one of the strongest emission lines of H<sub>2</sub> to arise in the K band and has been extensively used to map regions of shocked gas in molecular clouds (see for example Eislöffel 1997, for a recent review). Some unwanted features are also present in this emission map; some CCD columns to the right and left of the main central object chain show vertical and narrow linear emission structures that stand above the background noise level. These are probably due to the combined effect of poor cancellation of sky lines (due to the intrinsic sky emission line intensity changing over the integration period) in the reduction procedure and to the slight movements of the grating after changing (wavelength) position. The wavelength position of these features were compared with the list of OH airglow emission lines given in Olivia and Origlia (1992) and can be positively identified with the residual sky emission lines left over from the reduction procedure. This allows to check the on-line (mechanical) wavelength calibration (usually precise to  $\sim 1$  pixel). Using the two brightest OH lines in our spectra at 2.11710  $\mu\text{m}$  [(9,7)  $R_1(2)$ ] and 2.12440  $\mu\text{m}$  [(9,7)  $R_1(1)$ ], we have calculated the deviation of their profile centroids to the ones listed in Oliva & Origlia (1992). This gives a r.m.s. deviation error of 0.46 pixels and therefore imply an asso-

ciated uncertainty of  $\approx 30 \text{ km s}^{-1}$  for the measured radial velocities.

Apart from the continuum emission that is associated with the HH46 reflection nebula near the infrared source located close to the middle of the frame (rows  $\sim 22\text{--}25$ ), there are several objects clearly seen as bright emission knots aligned vertically in the middle of the array. These objects are labeled in Figure 2 and their relative positions can be identified using the maps of Eislöffel et al. (1994) and Micono et al. (1998).

Figure 2 shows the northeastern blueshifted outflow to be mainly composed of two bright emission knots, HH46 and HH47A. In the middle of the frame, HH46 appears as a bright knot blended with the nebular continuum emission from the ‘‘reflection nebula’’ centered at  $\sim$  row 24. The emission from HH46 appears blueshifted with a heliocentric radial velocity of about  $-70 \text{ km s}^{-1}$ , which is at the lower end of the radial velocities measured for [SII] and H $\alpha$  emission (Dopita et al. 1982, Meaburn & Dyson 1987, Reipurth & Heathcote 1991, Hartigan et al. 1993, Morse et al. 1994) which lies in the range  $\approx -80$  to  $-170 \text{ km s}^{-1}$ .

Further north, at the top of the PV map, there is a bright knot which we associate with the infrared counterpart of the high-excitation HH47A object. This object is commonly associated with the brightest working surface of the northeastern outflow and is located at a distance of about 65'' northward of HH46. The centroid velocity of this bright emission peak is seen at a heliocentric radial velocity of about  $-100 \text{ km s}^{-1}$ , which correlates well with the position of the optical, H $\alpha$  and [SII], emission knots seen blueshifted at  $\sim -80$  to  $-140 \text{ km s}^{-1}$  (Dopita et al. 1982, Meaburn & Dyson 1987, Hartigan et al. 1993, Morse et al. 1994). HH47A is considered the best example of a bow shock/Mach disk typical interaction, even though it is a secondary ejection from the source that is ploughing through a pre-accelerated and dense medium – the wake of an earlier shock now observed as HH47D. Imaging the HH47A shock in the near-infrared H<sub>2</sub> 1-0 S(1) line shows that it splits up in two regions: a bright knot Z and a fainter nebulosity to the south named as knot Y (Micono et al. 1998). In the region bridging HH46 to HH47A, there appears to be no significant H<sub>2</sub> emission in our maps, apart from the faint emission filament located north of HH46 and extending up to a distance of 20'' (rows  $\sim 25\text{--}32$ ) at essentially the same radial velocity. This is in good agreement with near-infrared maps; indeed, only a fainter emission patch can be seen to the west of the knot Z (Micono et al. 1998), which lies outside our slit. Even though this object lies at the edge of the frame, where the detector array may suffer from vignetting, we have, nevertheless, measured the line intensity and estimated the integrated column density for the brightest H<sub>2</sub> lines in this object (see Table 3).

The most striking feature of the H<sub>2</sub> near-infrared maps, however, is the bright and extended emission at the base of the redshifted outflow located south of HH46. This emission is associated with an extensive counter-jet shock clearly visible to the southwest of the HH 46/47 source in the H<sub>2</sub> 1-0 S(1) image presented by Eislöffel et al. (1994). This highly collimated counter-jet is not detected in H $\alpha$  emission and was only discovered by Reipurth and Heathcote (1991) in their [SII]  $\lambda\lambda 6716/6731\text{\AA}$  emission map as being composed of three emission knots extending 11'' on the sky.

The counter-jet faint appearance in the optical is probably due to the increased extinction at optical wavelengths and the fact that the counter-flow is moving towards the interior of the Bok globule. However, it is readily seen as the brightest object in our near-infrared PV maps since the extinction decreases about an order of magnitude from optical to infrared wavelengths. This counter-jet is known to be at the base of a larger (infrared) bow-shock that extends deeper into the interior of the Bok globule for about  $2'$  until it escapes out of the globule at HH47C (also seen in the infrared; e.g. Eislöffel et al. 1994). Figure 2 shows the counter-jet to be resolved in to *two* spatially blended emission knots but that appear clearly displaced in heliocentric radial velocity. The extent of this counter-jet is  $22''$  on the sky or  $0.037$  pc at the distance of HH46/47 (using a distance to the globule of  $350$  pc, Micono et al. 1998). The peak-to-peak separation of these knots is  $0.015$  pc ( $8.8''$  on the sky) which correcting for projection effects of the outflow orientation angle with respect to the plane of the sky ( $\sim 35$  degrees, Eislöffel and Mundt 1994) gives a separation distance of  $0.026$  pc.

The most interesting feature seen in the counter-jet is the apparent radial velocity separation of the two knots. Using the nomenclature of Micono et al. (1998), we identify the peak closer to the IR source as “c-jet a” which we will refer hereafter as the Counter-jet North, and “c-jet b+c+d” as the jet formed by three knots (unresolved in our images) which correspond to the southern knot and we will refer to it as the Counter-jet South. The brightest emission peak, Counter-jet North, appears at a distance of  $\sim 15''$  from HH46 with the emission centered at a heliocentric radial velocity of  $\sim +27$  km s $^{-1}$ , suggesting that the counter-jet starts moving near the systemic velocity of the globule as it travels away from the source and gradually increases its radial velocity by  $\approx 28$  km s $^{-1}$  within  $\sim 9''$  along the south-western emission lobe where the second peak, Counter-jet South, appears redshifted by  $\sim +55$  km s $^{-1}$ . We note also that this same pattern for acceleration of the gas is also seen in the proper motion data of Micono et al., where the proper motion knot shift is of order  $0.082$  arcsec yr $^{-1}$  for knot c-jet a (Counter-jet North) and  $0.138$  arcsec yr $^{-1}$  for knot c-jet d (farthest part of Counter-jet South).

We have also detected some emission at the southern edge of the slit (row 1) which we identify as “knot 5” in the nomenclature of Eislöffel et al. (1994, see Fig. 2a) or “knot g” using the latest near-infrared mapping of this region (Micono et al. 1998). We note that the position of this knot in the PV map suggests that the redshifted jet is flowing at essentially the same heliocentric radial velocity as the Counter-jet South knot.

Although the counter-jet flow shows up very brightly in the H $_2$  1-0 S(1) line emission map, it gets fainter with higher excitation energy of the H $_2$  levels (see Fig. 3). Note how the counter-jet is just barely visible in the 2-1 S(2) emission map and completely disappears on the noise in the 3-2 S(3) emission map. The H $_2$  2-1 S(1) contour emission map reveals that the counter-jet is still well defined, showing the same characteristic “double peak” shape as in the 1-0 S(1) map. Some fainter emission is still visible at the HH47A position but HH46 is now barely seen above the continuum emission from the reflection nebula. The H $_2$  1-0 S(0) emission map is very similar to the 1-0 S(1) map with HH46 standing well out from the nebular continuum. This map also

shows some residual OH lines that could not be perfectly subtracted from the final reduced object frame. However, this does not affect the flux measurements in Section 3.2 since the OH lines are non-coincident with the H $_2$  line. The emission maps obtained for the 3-2 S(1) and 4-3 S(3) lines (not shown) show substantially fainter emission from these objects implying a lack of high excitation H $_2$  in the gas since these lines arise predominantly from hot spots in the flow where the temperature is high enough to populate significantly the upper energy levels of the H $_2$  molecules.

Given this, further analysis is thus restricted to the brightest four lines, 1-0 S(1), 2-1 S(1), 1-0 S(0) and 3-2 S(3). Table 3 shows the physical parameters of these H $_2$  lines used in this work.

In order to fully investigate the emission spectra from the counter-jet we coadded all the detector rows comprising the entire counter-jet flow (rows 10–20) and fitted simultaneously two gaussians to the resulting spectra. Thus, the reference to Counter-jet North, in column 1 of Table 4, refers to the gaussian solution to the fit of the emission peak closer to the source whereas the reference to Counter-jet South refers to the gaussian solution to the fit of the emission peak far from the source. The reference to the Counter-jet Total was obtained by fitting a single gaussian profile to the spectra but allowing a broader FWHM to account for the line blending. The computed three-fold H $_2$  line fluxes from the counter-jet are presented in Table 4.

We have also searched for Brackett- $\gamma$  emission from the counter-jet, but nothing was found. The  $2.166$   $\mu$ m map only showed very weak continuum emission near the position of HH46 suggesting that the observed infrared emission is produced mainly by dust scattering in the diffuse reflection nebulae associated with HH46.

### 3.2 H $_2$ excitation temperature

The physical conditions for the excitation of H $_2$  emission can be quantified by calculating the H $_2$  level populations that are excited in the gas. Since H $_2$  is a homonuclear molecule it may only be excited through electric quadrupole radiation. In these conditions it is usual to assume the gas to be optically thin at these wavelengths, greatly simplifying the radiation transfer. Thus, the line intensity,  $I_{v,J}$ , for an H $_2$  transition out of level  $(v, J)$ , is directly proportional to the transition energy,  $h\nu_{v,J}$ , the Einstein coefficient,  $A_{v,J}$  and the column density  $N_{v,J}$  of molecules excited in that particular level,

$$I_{v,J} = h\nu_{v,J}A_{v,J}N_{v,J}/4\pi$$

where  $h$  is Planck’s constant and  $\nu$  is the transition frequency. The values for  $A_{v,J}$  are those from Turner et al. (1977) and the values for  $\nu_{v,J}$  are taken from Dabrowski (1984). For a Boltzmann distribution of the vibration-rotation levels (thermal distribution) at some local excitation temperature  $T_{\text{ex}}$ , the population density,  $N_{v,J}$ , of level  $(v, J)$ , is proportional to the statistical weight (level degeneracy)  $g_{v,J}$  and the Boltzmann factor. Thus,

$$N_{v,J} = g_{v,J} e^{-\frac{E_{v,J}}{kT_{\text{ex}}}}$$

where  $E_{v,J}$  is the transition energy,  $k$  is Boltzmann’s constant and  $T_{\text{ex}}$  is the excitation temperature. The excitation temperature can now be estimated from the data by

plotting  $N_{v,J}/g_{v,J}$  versus the upper level energy of the transition  $E_{v,J}$ . The coefficient of the exponential fit to this column density excitation diagram is proportional to  $T_{\text{ex}}^{-1}$ .

Figure 4 shows the H<sub>2</sub> excitation diagrams calculated for the counter-jet emission using the data in Table 4. Since the counter-jet appears spatially extended and constituted by two emission peaks with different velocity components, we have plotted in Fig. 4 three separate data sets corresponding to the total flux emission from the whole counter-jet (Counter-jet Total), the northern peak (Counter-jet North) and southern peak (Counter-jet South) emission. The excitation temperature,  $T_{2,1}$ , indicated by the 1-0 S(1) to the 2-1 S(1) line ratio in the Counter-jet North position is 2100 K while in the Counter-jet Total position it is 1800 K (see Table 4). A lower value of 1300 K is found for the Counter-jet South position. In Figure 4, the solid line represents a least square fit through all the data points, providing an excitation temperature of  $T_{\text{ex}} = 2600$  K for the H<sub>2</sub> gas at both the Counter-jet North and Total positions. The typical error of these estimates is given by the least squares fit and is of the order of 300 K.

Also shown in Table 4 are the H<sub>2</sub> line intensities and corresponding column densities for the HH46 and the HH47A objects. Unfortunately, at these positions the low signal-to-noise obtained in the higher excitation transitions ( $v \gtrsim 3$ ) hampers a more accurate determination of the excitation temperature. The excitation temperature for these objects are  $T_{2,1}=1200$  K and  $T_{2,1}=1800$  K for the HH46 and HH47A objects, respectively.

### 3.3 The [Fe II] emission

The forbidden emission from [Fe II] at  $1.257 \mu\text{m}$  ( $a^4D_{7/2} - a^6D_{9/2}$ ) and  $1.644 \mu\text{m}$  ( $a^4D_{7/2} - a^4F_{9/2}$ ) was observed on the third night at the same slit position used for the H<sub>2</sub> line observations to seek higher excitation regions within the flow and also to provide an estimate of the foreground extinction in the emitting gas. The position-velocity emission maps obtained for these two transitions are shown in Figure 5. Superposing both maps on a constant velocity grid makes all the bullet features coincide to within half pixel which gives an indirect way of checking the spatial shift correction performed on these maps. Since these [Fe II] PV maps show important morphological and kinematical differences from the H<sub>2</sub> maps presented previously, we will next examine them in detail.

In the northeastern blueshifted outflow region, we see from Fig. 5, that this part of the flow appears composed of four bright [Fe II] knots with  $V_{\text{Hel}} \sim -250$  to  $-280 \text{ km s}^{-1}$ , from which the northern most is clearly (spatially) associated with the HH47A object (at the top edge of the array in the [Fe II]  $1.644 \mu\text{m}$  map due to the spatial shift occurred when changing grating positions). This confirms the detection made by Eislöffel et al. (1994) of a strong near-infrared [Fe II]  $1.644 \mu\text{m}$  emission peak at the position of the optical HH47A object. We note that the radial velocity of the emitting [Fe II] in the HH47A object ( $-250 \text{ km s}^{-1}$ ) is much greater than the corresponding H<sub>2</sub> emission at  $-100 \text{ km s}^{-1}$ . On the other end, and at the base of this blueshifted outflow, the HH46 object shows up brightly against a very weak continuum. However, the most remarkable features in this Figure, are the appearance of *two* emission [Fe II] knots in the

northeastern part of the HH 46/47 jet, in the region bridging HH46 to HH47A, contrasting sharply with the morphology presented by the H<sub>2</sub> emission maps (Figs. 2–3). These two knots appear closer to HH46 and their locations in the outflow seem to have some parallel with the optical emission. Several high-resolution optical images of this part of the outflow have been published that show detailed structure across the whole region, from the base of the outflow at HH46, passing through the bright HH47A knot and ending in the HH47D object (Reipurth and Heathcote 1991, Hartigan et al. 1993, Eislöffel and Mundt 1994, Heathcote et al. 1996). The [Fe II] maps presented here show the existence of two relatively bright knots in this part of the outflow which we can tentatively identify with the optical knot B8 located at a distance of about  $18''$  from HH46 (Eislöffel and Mundt 1994), and knot B0 (HH47B), located at a distance of about  $32''$  from HH46 (see Figure 6). This is in contrast with the faint H<sub>2</sub> outflow which appears, in this region, to fade away at approximately the position of the B8 [Fe II] knot. Thus, it appears that the [Fe II] emission is tracing a higher velocity outflowing jet component with no relation to the lower velocity H<sub>2</sub> jet. The whole northern [Fe II] outflow appears blueshifted at heliocentric radial velocities between  $V_{\text{Hel}} \sim -280 \text{ km s}^{-1}$  (HH46, B8 and HH47B) and  $V_{\text{Hel}} \sim -250 \text{ km s}^{-1}$  (HH47A).

The [Fe II]  $1.644 \mu\text{m}$  emission was first observed in this object by Eislöffel et al. (1994, see Fig. 2a). Their emission map, however, shows a slightly different spatial distribution of [Fe II]  $1.644 \mu\text{m}$  emission, especially regarding the HH47B object. While the blueshifted knots associated with HH46 and B8 coincide in both maps, knot HH47B was not detected in their contour map. Two reasons might explain this fact. Either our map is slightly more sensitive or the evolution of the gas emission over time may have determined the fading of the emission knot. Either way, we note that both emission knots are clearly visible in our [Fe II]  $1.644 \mu\text{m}$  and [Fe II]  $1.257 \mu\text{m}$  maps and are both above ( $2\sigma$ ) the noisy sky background. Overall, the spatial morphology of our [Fe II]  $1.644 \mu\text{m}$  PV map closely matches the [Fe II]  $1.644 \mu\text{m}$  image map of Eislöffel et al. although, the emission in our image is clearly more extended and brighter along the main blueshifted outflow axis.

Turning to the southwestern region, there is a redshifted bright knot which is clearly associated with the emission from the counter-jet. As seen earlier, this counter-jet emission is elongated and marginally resolved in to *two* H<sub>2</sub> knots. However, we now see the [Fe II] emission from the counter-jet as a *single* redshifted knot at  $V_{\text{Hel}} = +100 \text{ km s}^{-1}$ . Moreover, when we overlay the H<sub>2</sub> and [Fe II] emission (see Figures 6 and 7), we conclude that this [Fe II] knot is associated with the Counter-jet North peak and that no [Fe II] emission is seen from the Counter-jet South peak. Notice also how this [Fe II] knot seems to appear marginally closer to the outflow source than to the bright Counter-jet North H<sub>2</sub> knot (c.f Figure 7) while it appears to be travelling substantially faster than the corresponding H<sub>2</sub> knot.

#### 3.3.1 Reddening

The extinction can be calculated using the relative flux observed from the [Fe II] transitions since these two lines arise from a common upper level of the Fe<sup>+</sup> ion ( $a^4D_{7/2}$ ) and the

line ratio is therefore independent of the number of excited ions on that particular level state. Thus, their intensity line ratio,  $I_{1.257}/I_{1.644}$ , should depend only on the intrinsic properties of the  $\text{Fe}^+$  ion, provided that the lines are optically thin. This requirement should be true since the critical density for the  $[\text{Fe II}]$  1.644  $\mu\text{m}$  transition is  $n_{crit} \sim 3 \times 10^4 \text{cm}^{-3}$  (Oliva, Moorhood and Danzinger 1990). The differential reddening between the two  $[\text{Fe II}]$  lines,  $E_{J-H}$ , can be computed from:

$$I_{1.257}/I_{1.644} = (I_{1.257}/I_{1.644})_0 \times 10^{-E_{J-H}/2.5}$$

where  $(I_{1.257}/I_{1.644})_0$  is equal to 1.36; the theoretical line ratio given by the Einstein spontaneous probabilities of Nussbaumer & Storey (1988). The visual extinction is obtained using  $E_{B-V} \approx 3 \times E_{J-H}$  (Draine 1989) and assuming a normal reddening law:  $A_V = 3.1 \times E_{B-V}$ . The derived  $[\text{Fe II}]$  line flux and extinction estimates are shown in Table 2 for the observed emission peaks. This table shows that the  $[\text{Fe II}]$  bullet associated with the Counter-jet North has a visual extinction of  $7.05 \pm 2.26$  whereas an extinction value of  $9.38 \pm 1.49$  is measured in the bullet associated with HH46, closer to the obscured YSO. Given the errors, these values indicate that the extinction is uniform throughout the region.

Note also that we measure  $A_V \sim 0$  for the northern  $[\text{Fe II}]$  bullets B8 and HH47B; given the uncertainties associated with the low flux measured for these bullets. This strongly suggests that the visual extinction is negligible in this (blueshifted) northwestern part of the outflow. However, as noted by Oliva and Origlia (1992), the  $[\text{Fe II}]$  1.644  $\mu\text{m}$  transition sits close ( $\sim 40 \text{km s}^{-1}$ ) to the relatively bright OH (5,3)  $R_1(2)$  transition which hampers a more accurate determination of the reddening.

#### 4 DISCUSSION

The intensity ratio of the  $v=1-0$  S(1) line to the  $v=2-1$  S(1) line has been widely used to discriminate between two common types of physical mechanisms for the excitation of HH objects: thermal (shocks) and non-thermal (e.g. fluorescence by Lyman- $\alpha$  or UV continuum pumping,  $\text{H}_2$  reformation). HH objects are preferentially shock excited but fluorescent excitation by Lyman- $\alpha$  pumping may also be present (HH43; Böhm, Scott and Solf 1991, HH47A; Curiel et al. 1995, HH7; Fernandes and Brand 1995). The 1-0/2-1 S(1) ratio derived from the observations (Table 5) for the Counter-jet Total, Counter-jet North and HH47A objects are  $15.7 \pm 2.3$ ,  $10.1 \pm 3.5$  and  $16.4 \pm 2.5$ , respectively. These values are consistent with shock excitation (in which the 1-0/2-1 S(1) ratio  $\gtrsim 5$ ) as fluorescent excitation requires the 1-0/2-1 S(1) ratio to be  $\lesssim 2$  in low density regions. In high density regions the fluorescence 1-0/2-1 S(1) ratio may be  $\gg 2$ . However, this is unlikely to be the case here, since these high density models predict large column densities in the  $v=3$  and  $v=4$  levels and thus strong emission from lines such as the 3-2 S(3) and 4-3 S(3) which could not be observed from the data. Under these conditions, the molecular hydrogen emission has its origin behind dense shocks and the  $\text{H}_2$  excitation diagrams calculated for the HH objects (Figure 4) are consistent with thermalised gas at a temperature of  $T_{2,1} \approx 1300\text{--}2100$  K for

the counter-jet whereas HH46 and HH47A display  $T_{2,1} \approx 1200$  and  $1800$  K, respectively. We note here that non-LTE, low density gas, may also produce line ratios similar to those observed here, as we will discuss below.

The densities required to thermalise the  $\text{H}_2$  levels up to 20 000 K are of order  $10^6\text{--}10^7 \text{cm}^{-3}$  in a pure molecular gas (Burton et al. 1989). These high densities can be attained in regions close to the source from where the counter-jet emerges or in the dense relaxation medium behind the shock front where the gas cools via atomic, ionic and molecular line emission. Both pure hydrodynamic shocks (J-type) and magneto-hydrodynamic shocks (MHD C-type) can produce significant emission from  $\text{H}_2$ , although only fast (dissociative) J-type shocks can produce observable  $[\text{Fe II}]$  emission since C-shocks attain a lower post-shock temperature ( $\lesssim 2000$  K) than J-shocks ( $\gg 2000$  K).

Comparing the 1-0/2-1 S(1) line ratios with the shock models of Smith (1995) and Eisloffel et al. (1996) yields a useful constraint on the various critical shock parameters such as the pre-shock density and the type and geometry of the shock. First, note from Table 5 that the observed range for the line ratios of 10–17 (except for the noisier Counter-jet South and HH46 objects) is consistent with a slow planar J-shock with speed  $8\text{--}9 \text{km s}^{-1}$ . However, these line ratios can be also reproduced by fast planar C-shocks with speeds of  $35\text{--}40 \text{km s}^{-1}$ . The modelled 1-0 S(1)/3-2 S(3) line ratio of 447.7 for a  $35 \text{km s}^{-1}$  C-shock is nonetheless much greater than the observed value of only 45–50 and thus planar C-shocks can be ruled out. On the other hand, the slow J-shocks are much weaker than those required to excite the observed  $[\text{Fe II}]$  lines as we will see below. On these grounds, we conclude that neither *planar* type of shock can explain the observations, except, perhaps, for the Counter-jet South and HH46 objects from which no conclusions can be drawn due to the large errors in the observed line ratios.

Constant temperature models were also compared with the observations. The single (1T) and mixed temperature (2T) slab of gas models for both LTE ( $n=10^8 \text{cm}^{-3}$ ) and non-LTE conditions ( $n=10^4 \text{cm}^{-3}$ ) yield specific line ratios which are given in Table 5 (Smith, private communication). The three chosen 1T models in Table 5 fail to account for both line ratios regardless of the LTE conditions. Moreover, the excitation temperature derived from the 1-0/2-1 S(1) line ratio ranges 1800–2100 K, whereas the least square fit to all the data points implies a higher excitation temperature of 2600 K. Given this, we may expect better results from the dual temperature models. In fact, an inspection of Table 5, clearly indicates a closer match to the data. However, there are strong physical constraints on these approach since we would need a heating mechanism capable of maintaining the gas at fixed temperatures of order of a few thousand Kelvin for a timescale of years. At present, there is no valid explanation for such mechanism, and thus we also rule out this possibility.

In agreement with the observed morphology for these type of objects, we thus turn our attention to the excitation of both  $\text{H}_2$  and  $[\text{Fe II}]$  emission in bow-shock models. Strong  $[\text{Fe II}]$  emission is often interpreted as indicative of shock excitation (e.g Moorwood & Oliva 1988) and can be expected in, for example, supernova remnants (McKee, Chernoff & Hollenbach 1984). In bow-shocks, however, the high excitation  $[\text{Fe II}]$  emission derives from the bow-head,

where the shock is strongest (see e.g. HH1; Davis, Eisloffel & Ray 1994). Further downstream, in the lower excitation oblique bow wings, emission from H<sub>2</sub> can be excited in the softer (non-ionising) shocks. The presence of [Fe II] 1.644 μm in the flow is thus considered a diagnostic of fast dissociative shocks at the tip of the bullet that heads a post-shocked and accelerated medium observed as a trailing H<sub>2</sub> wake (see e.g. Tedds, Brand and Burton 1998).

The bow shock emission structure can be modelled by a surface of revolution which can be simply written as  $z \propto r^s$  in cylindrical coordinates, where  $s$  is the free parameter that adjusts the bow aperture (see Fig. 6 of Eisloffel et al. 1996). This morphology combines in a single structure, two distinct regions, depending on the local physical conditions, especially the ion fractions and the strength of the magnetic field. Thus, we need to distinguish between J-type or C-type bow shocks.

The former, produces emission which is everywhere excited by pure hydrodynamic type shocks, from the apex of the bow, where strong J-shocks destroy the H<sub>2</sub> molecules and ionises Fe, to the extended H<sub>2</sub> emitting wings downstream along the surface. The predictions from these bows depend critically on the shape parameter  $s$ . The best parameter fit models are shown in Table 5. In general, both LTE and non-LTE models come close to adjust the observed line ratios. The best fit bow shape parameter in these models range from 1.2 to 2.0 (paraboloidal) which is consistent with strong [FeII] emission over much of the outflow. Narrow line profiles are expected from these type of shocks and can be used to discriminate between shock types, since the larger shock front of C-type shocks will produce wider line profiles. This, however, requires high-resolution spectroscopy data and therefore with the present set of data we cannot rule out the J-shock bow model for the Counter-jet or HH47A.

On the other hand, the C-type bow shock model differs from the above picture only on the bow wings, where the softer C-type shocks produces emission from H<sub>2</sub> and CO. The Orion bullets are the best studied example of this structure, where a high-velocity leading [Fe II] bullet is ploughing through the medium leaving behind a wake of lower-excitation H<sub>2</sub> emitting gas generated at the warmer and oblique C-type shocks at the bow flanks (Tedds, Brand and Burton 1999). The C-type bow-shock model fits shown in Table 5 can also be made to agree with the present line ratios, but for a larger  $s$  bow shape parameter ( $1.5 < s < 2.0$ ). In this case, the bows are closer to paraboloids and less pointed than the J-type bows.

The [Fe II] 1.644 μm surface brightness predicted for a fast ( $v > 30 \text{ km s}^{-1}$ ) J-shock can be large due to the large column of warm gas generated by UV absorption and H<sub>2</sub> reformation in the post-shock layer (Smith 1994). For a  $100 \text{ km s}^{-1}$  shock with a pre-shock density of  $10^4 \text{ cm}^{-3}$ , a surface brightness of  $1.5 \times 10^{-4} \text{ erg s}^{-1} \text{ cm}^{-2} \text{ sr}^{-1}$  for the [Fe II] 1.644 μm line can be achieved. This value is consistent within a factor of 3 with our measured value at the Counter-jet North peak of  $4.6 \times 10^{-4} \text{ erg s}^{-1} \text{ cm}^{-2} \text{ sr}^{-1}$ . Note that this is as strong as the observed H<sub>2</sub> 1-0 S(1) surface brightness of  $4.4 \times 10^{-4} \text{ erg s}^{-1} \text{ cm}^{-2} \text{ sr}^{-1}$ . Such high values, where the [Fe II] 1.644 μm / H<sub>2</sub> 1-0S(1) line ratio are of equal strength, have already been observed in other HH objects by Stapelfeldt et al. (1991) and can be well modelled with fast J-shock models (Smith 1994).

A non-dissociative J-shock ( $v \lesssim 22 \text{ km s}^{-1}$ ), on the other hand, produces smaller columns of warmer gas. We may estimate an upper limit for the [Fe II] 1.644 μm line strength from the model employed by Smith (1994) under the assumptions that the electron fraction is  $\sim 10^{-3}$  and the abundance of Fe<sup>+</sup> is  $\sim 10^{-6}$ . For the fastest non-dissociative shock (with  $v = 22 \text{ km s}^{-1}$ ), the line strength predicted is  $< 4.2 \times 10^{-5} \text{ erg s}^{-1} \text{ cm}^{-2} \text{ sr}^{-1}$ , a value which is about 10 times smaller than observed. For a  $15 \text{ km s}^{-1}$  shock speed, the [Fe II] 1.644 μm intensity drops down by a factor of 2 and therefore we rule out the slow J-shock model for the generation of excited [Fe II].

Downes (1997) has modelled the H<sub>2</sub> and [SII] λ6731 emission from the HH 46/47 counter-jet using an hydrodynamical code to predict intensity maps and line profiles. The simulated emission showed the appearance of numerous mini-bowshocks throughout the outflowing jet resulting from Rayleigh-Taylor instabilities. Moreover, the synthesised [SII]λ6731 and H<sub>2</sub> 1-0 S(1) line profiles derived from their emission maps of the counter-jet, yield clear asymmetries in the profiles with the near-infrared line peaking at  $3\text{--}4 \text{ km s}^{-1}$ , while the optical line peaks at about  $150 \text{ km s}^{-1}$ . Since the H<sub>2</sub> emission appears only at the bow flanks, it displays a low velocity component; in our data +27 and +55  $\text{km s}^{-1}$ , for the Counter-jet North and South objects, respectively. In contrast, the [Fe II] knot coincident with the Counter-jet North object, is seen peaking at a higher velocity of +100  $\text{km s}^{-1}$ . This agrees well with the bow shock scenario, where the high excitation lines of [FeII], [SII] and Hα, are produced in the strong and high speed shocks near the bow apex, yielding higher normal gas velocities of  $\sim 100\text{--}150 \text{ km s}^{-1}$ .

Looking at the relative position of the [Fe II] and H<sub>2</sub> emission in HH47A (see Figs. 6 and 7), we see the [Fe II] peak ahead about 5'' from the H<sub>2</sub> peak. The spatial calibration is accurate to less than half pixel ( $\sim 1''$ ) and thus we consider the shift to be genuine. This translates to a separation distance of  $\sim 3 \times 10^{16} \text{ cm}$  from the [Fe II] emitting section to the H<sub>2</sub> emitting section. This separation is characteristic in bow-shocks viewed at orientation angles  $> 30$  degrees to the line of sight (Smith 1991) and thus we suggest that HH47A can be well modelled by a bow shock working surface, in a similar fashion to HH99B (Davis, Smith & Eisloffel 1999). Note, however, the large radial velocities achieved for the [Fe II] ( $-250 \text{ km s}^{-1}$ ), Hα ( $-130 \text{ km s}^{-1}$ ) and even H<sub>2</sub> ( $-100 \text{ km s}^{-1}$ ), whose molecules should be all dissociated at these high ( $v \gtrsim 50 \text{ km s}^{-1}$ ) speeds. To produce H<sub>2</sub> emission at these extreme velocities, it is necessary that the pre-shock medium had already been set in motion by some previous event (e.g. through the passage of an earlier shock wave which may be accounted by the faint HH47D object), so that the relative velocity between the two flows stays lower than the dissociative limit of the H<sub>2</sub> molecule:  $25 \text{ km s}^{-1}$ , for a J-shock or  $50 \text{ km s}^{-1}$ , for a C-shock (Smith 1991). Unfortunately in this work, we have not reached the required sensitivity in the 3-2 S(3) line in HH47A to help discriminate between these two types of shocks spectroscopically. Thus, on geometrical grounds, we expect HH47A to be a classical bow shaped shock, with a dissociative J-shock section at the bow apex (which produces the [Fe II] and the optical emission), plus a longer C-shock wing section which produces the lower excitation H<sub>2</sub> emission. With the measured tangential

velocities in this object of the order  $\sim 180 \text{ km s}^{-1}$  (both optical and near-infrared), a bow shock velocity of  $\approx 220 \text{ km s}^{-1}$  can be inferred.

The emission from HH46 is partially blended with the reflection nebula which causes the  $\text{H}_2$  emission to be scattered and thus appear weaker in contrast to the brighter [Fe II] emission. The 2-1 S(1) line emission from HH46 is somewhat below our expectations since the 1-0 S(1) remains strong. In fact, the 2-1/1-0 S(1) line ratio is only 0.014 compared with, for example, 0.061 in HH47A. We suggest that we may be observing only the emission tail of HH46, which produces weaker shocks, and thus explaining the weaker  $\text{H}_2$  2-1 S(1) emission observed and also the  $-70 \text{ km s}^{-1}$  heliocentric velocity shift observed for this object. Moreover, the [Fe II] emission peaks at  $-280 \text{ km s}^{-1}$ , implying very fast bow shock speeds near the source. In fact, a shock which produces [Fe II] efficiently, will likely destroy the  $\text{H}_2$ . For  $\text{H}_2$  to survive the extreme shock velocities observed in HH46, we therefore require a mechanism that can soften the shock. Commonly cited in the literature are mechanisms such as the magnetic precursor model, the entrainment of material from the wind/ambient material interface or the high Alfvén Mach number shock absorbers (bow shocks with a high magnetic field). Distinguishing between these physical processes is beyond the scope of this paper with the available set of data. Obtaining higher resolution data will certainly help to establish the importance of these mechanisms.

## 5 CONCLUSIONS

The physical conditions along the redshifted counter-jet and the blueshifted HH46 to 47A outflow were investigated through observation of velocity-position diagrams and spectra in the J ([Fe II]  $1.644 \mu\text{m}$  and [Fe II]  $1.257 \mu\text{m}$ ) and K (several  $\text{H}_2$  transitions) infrared bands.

The observed  $\text{H}_2$  line emission confirms the existence of a bright and extended redshifted counter-jet outflow southwest of HH46. Moreover, there seems to be compelling evidence for acceleration of the counter-jet from  $27 \text{ km s}^{-1}$  to  $55 \text{ km s}^{-1}$  along the southwestern emission lobe as it travels away from the source.

The observed [Fe II] emission suggests a near uniform extinction in the HH46 and the counter-jet region of  $\approx 7-9$  visual magnitudes, whereas the extinction calculated for the blueshifted knot B8 and HH47B objects is negligible.

The  $\text{H}_2$  excitation temperatures derived from the 1-0/2-1 S(1) ratio are in the range 1800–2100 K for all the objects, with the exception of the HH46 object for which the excitation temperature is 1200 K. The unusual low 2-1 S(1) line flux in this object was probably caused by the limited region covered by our slit in this object which may have sampled only the wing sections of the bow-shock structure. The inclusion of the 3-2 S(3) in the  $\text{H}_2$  excitation diagrams for the counter-jet shock yields an excitation temperature for the gas of  $T_{\text{ex}} \approx 2600 \text{ K}$ .

The non-detection of higher energy transitions of  $\text{H}_2$  in the K band, precludes several non-thermal excitation mechanisms such as fluorescence or  $\text{H}_2$  reformation. The observed 2-1/1-0 S(1) and 3-2/1-0 S(1) line ratios were found consistent with models of J and C-type bow shocks, whilst

ruling out planar shocks. In the counter-jet, the shape parameter for C-type bows can be constrained to the range  $1.5 < s < 2.0$  whereas J-type bows need to be made extremely wide,  $1.2 < s < 1.5$ , to adjust well our data.

## ACKNOWLEDGEMENTS

This work was supported by the Portuguese Fundação para a Ciência e Tecnologia (grant PESO/P/PESO/1196/97). I thank Chris Davis and Michael Smith for some helpful suggestions to improve this manuscript.

## REFERENCES

- Böhm K., Scott D. and Solf J. 1991, *ApJ*, 371, 248  
 Curiel S., Raymond J., Wolfire M., Hartigan P., Morse J. Schwartz R. and Nienson P. 1995, *ApJ*, 453, 322  
 Burton M., Brand P., Geballe T. and Webster A. 1989, *MNRAS*, 236, 409  
 Davis C., Eisloffel J. and Ray 1994, *ApJL*, 422, L91  
 Davis C. and Smith M. 1995, *A&A*, 443, L41  
 Davis C.J., Smith M.D., Eisloffel J. and Davies J.K., 1999, *MNRAS*, 308, 539  
 Dabrowski I. 1984, *CPJ*, 62, 1179  
 Dopita M., Schwartz R. and Evans I. 1982, *ApJL*, 263, L73  
 Downes T. 1997, *Irish Astronomical Journal*, 24, 31  
 Draine B. 1989, in *22<sup>nd</sup> Eslab Symposium on Infrared Spectroscopy in Astronomy*, ESA SP-290, pp 93–98, ESA Publications Ltd, Salamanca, December 7–9  
 Eisloffel J. 1997, in B. Reipurth and C. Bertout (eds.), *Herbig-Haro flows and the birth of low mass stars*, No. 182 in IAU Symposium, pp 93–101, International Astronomical Union, Kluwer academic publishers  
 Eisloffel J., Smith, M., Davis C. and Ray T., 1996, *AJ*, 112, 2086  
 Eisloffel J., Davis C., Ray T., and Mundt R. 1994, *ApJL*, 422, L91  
 Eisloffel J. and Mundt R. 1994, *A&A*, 284, 530  
 Fernandes A. and Brand P. 1995, *MNRAS*, 274, 639  
 Graham J. and Elias J. 1983, *ApJ*, 272, 615  
 Gredel R. and Moorwood A. 1991, *ESO Operating Manual No. 10*  
 Hartigan P., Raymond J and Meaburn J. 1990, *ApJ*, 362, 624  
 Hartigan P. and Morse J. and Heathcote S. and Cecil G. 1993, *ApJ*, 414, L121  
 Heathcote S., Morse J.A., Hartigan P., Reipurth B., Schwartz R., Bally J., and Stone J. 1996, *AJ*, 112, 1141  
 Meaburn J. and Dyson E. 1987 *MNRAS*, 255, 863  
 Micono M., Davis C., Ray T., Eisloffel J. and Shetrone M. 1998, *ApJL*, 494, L227  
 Moorhood A., Moneti. A., and Gredel R. 1991, *The Messenger*, 63, 77  
 Morse J., Hartigan P., Heathcote S., Raymond J. and Cecil G. 1994, *ApJ*, 425, 738  
 Noriega-Crespo A., Garnavich P., Curiel S., Raga A., and Ayala S. 1997, *ApJL*, 486, L55  
 Nussbaumer H. and Storey P. 1988, *A&A*, 193, 327  
 Oliva E., Moorwood A., and Danzinger I. 1989, *A&A*, 240, 453  
 Oliva E. and Origlia L. 1992, *A&A*, 254, 466  
 Reipurth B. and Heathcote S. 1991, *A&A*, 246, 511  
 Schwartz R. 1977, *ApJ*, 212, L25  
 Schwartz R., Jones B. and Sirk M. 1984, *AJ*, 89, 1735  
 Smith M. 1991, *MNRAS*, 252, 378  
 Smith M. 1994, *A&A*, 289, 256  
 Smith M. 1995, *A&A*, 296, 789

Stapelfeldt K., Beichmann C., Hester J., Scoville N. & Gautier  
III T. 1991, ApJ, 371, 226  
Teds J., Brand P. and Burton M. 1999, Aug 1st MNRAS  
Turner J., Kirby-Docken K. and Dalgarno A. 1977, ApJS, 35, 281

This paper has been produced using the Royal Astronomical  
Society/Blackwell Science L<sup>A</sup>T<sub>E</sub>X style file.



**Table 1.** Parameter list of the observed emission lines

Species	Transition label	$\lambda_0$ ( $\mu\text{m}$ )	Total Exp. (min) <sup>a</sup>	Spatial Shift <sup>b</sup>	Resolution $\Delta v$ ( $\text{km s}^{-1}$ ) <sup>c</sup>
H <sub>2</sub>	1-0 S(1)	2.1218	3	0.0	66.8
H <sub>2</sub>	1-0 S(0)	2.2235	4	1.0	61.5
H <sub>2</sub>	2-1 S(1)	2.2477	8	1.5	60.3
H <sub>2</sub>	2-1 S(2)	2.154	5	0.5	65.1
H <sub>2</sub>	2-1 S(3)	2.065	3	-0.5	70.0
H <sub>2</sub>	3-2 S(1)	2.3846	8	2.5	53.6
H <sub>2</sub>	3-2 S(3)	2.2014	10	0.5	62.6
H <sub>2</sub>	4-3 S(3)	2.3445	8	2.5	55.5
H	Brackett- $\gamma$	2.166	5	0.5	64.5
[Fe II]	$a^6D_{9/2} - a^4D_{7/2}$	1.257	2	3.5	47.7
[Fe II]	$a^4F_{9/2} - a^4D_{7/2}$	1.644	1	-2.5	97.9

<sup>a</sup> This is the total exposure time of the final reduced frame.

<sup>b</sup> Spatial shift or displacement (in pixels) between frames due to the use of different grating settings which were calculated using observations of the standard star Eta Canis-Majoris at different wavelength settings.

<sup>c</sup> Velocity resolution per pixel calculated using the wavelength resolution:  $\Delta v/v = \Delta\lambda/\lambda$

**Table 2.** Line flux and extinction estimate towards HH46, the counter-jet and the [Fe II] bullets

Parameter	Counter-jet North	HH46	knot B8	HH47B
[Fe II] 1.257 $\mu\text{m}$	3.95 (0.87)	4.85 (0.67)	4.79 (0.77)	3.98 (0.87)
[Fe II] 1.644 $\mu\text{m}$	5.84 (0.22)	9.03 (0.45)	3.10 (0.30)	2.44 (0.34)
1.257/1.644	0.68 (0.15)	0.54 (0.08)	1.54 (0.29)	1.63 (0.42)
$E_{J-H}$	0.76 (0.24)	1.01 (0.16)	-0.14 (0.20)	-0.20 (0.28)
$A_{2.1218}$	0.78 (0.25)	1.04 (0.16)	-0.14 (0.21)	-0.20 (0.29)
$E_{B-V}$	2.27 (0.73)	3.03 (0.48)	-0.41 (0.61)	-0.59 (0.84)
$A_V$	7.05 (2.26)	9.38 (1.49)	-1.28 (1.90)	-1.83 (2.61)

Note: The line flux are in units of  $10^{-14} \text{erg s}^{-1} \text{cm}^{-2}$

**Table 3.** Physical parameters for the brightest H<sub>2</sub> lines

Transition	1-0 S(1)	1-0 S(0)	2-1 S(1)	3-2 S(3)
$\lambda_0$ ( $\mu\text{m}$ )	2.1218	2.2235	2.2477	2.2014
Energy (Kelvin)	6956	6471	12550	19086
Statistical weight <sup>a</sup>	21	5	21	33
Spontaneous decay rate <sup>b</sup>	3.47	2.53	4.98	5.63
Extinction ( $A_\lambda$ )	1.04	0.96	0.94	0.98

<sup>a</sup> The statistical weight is  $(2J+1)(2I+1)$ ; where  $J$  is the rotational quantum number and  $I$  is the spin quantum number

<sup>b</sup> Einstein coefficient in units of  $10^{-7} \text{s}^{-1}$

**Table 4.** Observed H<sub>2</sub> line intensities and derived column densities

Object	Transition label	Observed line intensity <sup>a</sup>	De-reddened line intensity <sup>b</sup>	N <sub>j</sub> /g <sub>j</sub> (cm <sup>-2</sup> ) <sup>c</sup>	T <sub>2,1</sub> <sup>ex</sup> (Kelvin) <sup>d</sup>	T <sup>ex</sup> (Kelvin) <sup>e</sup>
HH46	1-0 S(1)	280 (32)	57.4 (6.6)	105.8 (12.1)	1200	
	1-0 S(0)	33.5 (6.6)	6.5 (1.3)	72.3 (14.3)		
	2-1 S(1)	4.28 (2.25)	0.82 (0.43)	1.12 (0.59)		
	3-2 S(3)	< 21.8	< 4.3	< 3.2		
HH47A	1-0 S(1)	376 (29.9)	77.1 (6.1)	142.1 (11.3)	1800	
	1-0 S(0)	29.9 (5.5)	5.8 (1.1)	64.6 (11.9)		
	2-1 S(1)	24.5 (3.1)	4.7 (0.6)	6.4 (0.8)		
	3-2 S(3)	< 25.1	< 4.9	< 3.7		
Counter-jet North	1-0 S(1)	212.9 (58.5)	43.7 (12.0)	80.4 (22.1)	2100	2600
	1-0 S(0)	37.4 (5.8)	7.3 (1.1)	80.7 (12.5)		
	2-1 S(1)	22.5 (4.8)	4.3 (0.9)	5.9 (1.3)		
	3-2 S(3)	5.0 (2.3)	0.98 (0.45)	0.74 (0.34)		
Counter-jet South	1-0 S(1)	138.3 (58.9)	28.4 (12.1)	52.3 (22.3)	1300	
	1-0 S(0)	17.5 (4.45)	3.40 (0.86)	37.8 (9.6)		
	2-1 S(1)	2.91 (2.6)	0.56 (0.50)	0.76 (0.68)		
	3-2 S(3)	< 18.0	< 3.5	< 2.6		
Counter-jet Total	1-0 S(1)	364.1 (23.5)	74.7 (4.8)	137.6 (26.6)	1800	2600
	1-0 S(0)	54.6 (3.0)	10.6 (0.6)	117.9 (19.4)		
	2-1 S(1)	24.8 (3.2)	4.8 (0.6)	6.5 (2.5)		
	3-2 S(3)	7.9 (1.1)	1.6 (0.2)	1.2 (0.5)		

<sup>a</sup> Units of 10<sup>-6</sup> erg s<sup>-1</sup> cm<sup>-2</sup> sr<sup>-1</sup>

<sup>b</sup> Extinction corrected line intensities in units of 10<sup>-5</sup> erg s<sup>-1</sup> cm<sup>-2</sup> sr<sup>-1</sup> according to the values in Table 2

<sup>c</sup> Integrated column density divided by the number of degenerate levels (statistical weight) in units of 10<sup>13</sup> cm<sup>-2</sup>

<sup>d</sup> Excitation temperature calculated using the 1-0 S(1) to 2-1 S(1) line ratio

<sup>e</sup> Excitation temperature calculated using a least square fit to all the data points

**Table 5.** Line ratios compared with planar J and C-type shock models from Smith (1995).

Object or Model	$I_{1-0S(1)}/I_{2-1S(1)}$	$I_{1-0S(1)}/I_{3-2S(3)}$
HH46	70.0 (37.6)	> 13.4
HH47A	16.4 (2.5)	> 15.6
Counter-jet North	10.1 (3.5)	44.5 (23.8)
Counter-jet South	50.8 (50.3)	> 8.0
Counter-jet Total	15.7 (2.3)	48.1 (7.4)
Planar shocks		
Model J8	17.9	340
Model J9	10.0	88
Model J15	4.2	12.6
Model J22	3.51	< 10
Model C35	20.1	447.7
Model C40	10.9	122
Model C50	4.75	20
Constant single (1T) and dual (2T) temperature slabs		
Model 1T <sup>1</sup>	10	112
Model 1T	15	277
Model 1T	6.5	45
Model 2T <sup>2</sup>	10	50
Model 2T	15	100
Model 2T	9.6	45
Bow-shocks (J-type) <sup>3</sup>		
Model LTE	10	56
Model LTE	15	108
Model LTE	8.8	45
Model non-LTE, $2 \times 10^4 \text{cm}^{-3}$	10	48
Model non-LTE, $2 \times 10^4 \text{cm}^{-3}$	15	91
Model non-LTE, $2 \times 10^4 \text{cm}^{-3}$	9.6	45
Bow-shocks (C-type) <sup>4</sup>		
Model $10^6 \text{cm}^{-3}$	10	56
Model $10^6 \text{cm}^{-3}$	15	111
Model $10^6 \text{cm}^{-3}$	8.7	45
Model $10^4 \text{cm}^{-3}$	10	50
Model $10^4 \text{cm}^{-3}$	15	100
Model $10^4 \text{cm}^{-3}$	9.3	45
Model $10^8 \text{cm}^{-3}$	10	40
Model $10^8 \text{cm}^{-3}$	15	67
Model $10^8 \text{cm}^{-3}$	11	45

<sup>1</sup> LTE standard conditions,  $n=10^8 \text{cm}^{-3}$  (identical results are found for non-LTE conditions,  $n=10^4 \text{cm}^{-3}$ ).<sup>2</sup> Mixed 1600K (95%) plus 3500K (5%) gas.<sup>3</sup> Bow shape parameter:  $1.2 < s < 1.5$ <sup>4</sup>  $1.5 < s < 2.0$